Detecting a stochastic gravitational-wave background in the presence of correlated magnetic noise

Patrick M. Meyers, Katarina Martinovic, Nelson Christensen, Mairi Sakellariadou

Detecting a stochastic gravitational-wave background in the presence of correlated magnetic noise

Patrick M. Meyers,[1,2,*] Katarina Martinovic,[3,†] Nelson Christensen,[4,‡] and Mairi Sakellariadou[3,§]

[1]*School of Physics, University of Melbourne, Parkville, Victoria 3010, Australia*
[2]*OzGrav, University of Melbourne, Parkville, Victoria 3010, Australia*
[3]*Theoretical Particle Physics and Cosmology Group, Physics Department, King's College London, University of London, Strand, London WC2R 2LS, United Kingdom*
[4]*Artemis, Université Côte d'Azur, Observatoire de la Côte d'Azur, CNRS, Nice 06300, France*

(Received 3 August 2020; accepted 5 October 2020; published 13 November 2020)

A detection of the stochastic gravitational-wave background (SGWB) from unresolved compact binary coalescences could be made by Advanced LIGO and Advanced Virgo at their design sensitivities. However, it is possible for magnetic noise that is correlated between spatially separated ground-based detectors to mimic a SGWB signal. In this paper we propose a new method for detecting correlated magnetic noise and separating it from a true SGWB signal. A commonly discussed method for addressing correlated magnetic noise is coherent subtraction in the raw data using Wiener filtering. The method proposed here uses a parametrized model of the magnetometer-to-strain coupling functions, along with measurements from local magnetometers, to estimate the contribution of correlated noise to the traditional SGWB detection statistic. We then use Bayesian model selection to distinguish between models that include correlated magnetic noise and those with a SGWB. Realistic simulations are used to show that this method prevents a false SGWB detection due to correlated magnetic noise. We also demonstrate that it can be used for a detection of a SGWB in the presence of strong correlated magnetic noise, albeit with reduced significance compared to the case with no correlated noise. Finally, we discuss the advantages of using a global three-detector network for both identifying and characterizing correlated magnetic noise.

DOI: 10.1103/PhysRevD.102.102005

I. INTRODUCTION

During their first two observational runs, Advanced LIGO [1] and Advanced Virgo [2] detected gravitational-wave (GW) signals from ten binary black hole mergers, and one binary neutron star merger [3]. During the third observation run (O3), numerous low-latency alerts for binary black hole, binary neutron star, and neutron star–black hole mergers have been sent out to astronomers [4]. Exceptional events from O3 are now being published, including new compact binary mergers that could be neutron star–black hole mergers [5,6]. These detections have already made a broad-reaching impact on stellar astrophysics, the study of dense nuclear matter, and beyond. In the coming years, one of the main targets of ground-based interferometeric GW detectors will be a detection of the stochastic gravitational-wave background (SGWB). In this paper, we address a potential hurdle faced on the way to the eventual detection of such a background. We expect a SGWB from unresolved compact binary coalescences (CBCs) could be detectable by the time Advanced LIGO and Advanced Virgo reach design sensitivity [7]. Other sources, both astrophysical and cosmological, can contribute to the SGWB, the most exciting of which include GWs from the early Universe [8]. SGWB searches can also complement transient GW searches, through, e.g., searching for alternative polarizations of GWs [9–11], and can be used together with transient detections to constrain the star formation history of the Universe [12].

Unlike for transient signals, searches for a SGWB require long integration times because the signal is much smaller than the intrinsic detector noise. We search for the SGWB by cross-correlating outputs from two or more widely separated detectors, and when there are no correlated noise sources between the detectors, the only limiting factor of the search is total observation time [13,14]. In the presence of noise that is correlated between the detectors, however, we must accurately estimate and separate the relative strengths of the correlated noise and the SGWB.

Correlated noise in GW detectors caused by Earth's electromagnetic field, in the form of the Schumann resonances, could be comparable to the sensitivity of SGWB searches performed by the advanced detector network in

*pat.meyers@unimelb.edu.au
†katarina.martinovic@kcl.ac.uk
‡nelson.christensen@oca.eu
§mairi.sakellariadou@kcl.ac.uk

the near future [13,15,16]. Analytic models of the impact of correlated noise in GW detectors have been explored in recent work, such as [17,18]. Meanwhile, the focus of most attempts at mitigating the effects of correlated detector noise on SGWB searches has centered on Wiener filtering of the correlated signal using local environmental sensors [15,16,19,20]. In addition, a method for validating a potential SGWB signal once it is detected using geodesy [21] has also been proposed. The geodesy method provides a check on whether a proposed SGWB signal is consistent with an isotropic SGWB or if it is more consistent with environmental disturbances. Such a method offers complementary information to approaches that attempt to subtract or mitigate correlated noise.

In this paper, we take a different tact. We model the contribution of correlated magnetic noise from Schumann resonances to the frequency-domain SGWB estimator used by most searches [22]. We propose a method to simultaneously detect correlated magnetic noise and a SGWB using local on-site magnetometers and current SGWB search data products. We then demonstrate this method using realistic time-domain and frequency-domain synthetic datasets with varying levels of correlated magnetic noise. Such a method offers an alternative to Wiener filtering, but could also be used on data that has already had Wiener filtering subtraction applied, given that Wiener filtering in the low signal-to-noise regime can result in imperfect subtraction [20].

The rest of this paper is organized as follows. In Sec. II, we introduce the cross-correlation statistic used in SGWB searches, and highlight complications introduced by correlated detector noise. In Sec. III, we explain the Schumann resonances and their coupling to the detectors, and we present the way we model this coupling. We then present a method of simulating synthetic time series data that includes a correlated magnetic spectrum in a multidetector network. In Sec. IV, we discuss a model for the SGWB search statistic that includes correlated magnetic noise, and demonstrate how we use that model to codetect the presence of correlated magnetic noise and a SGWB. We present results on synthetic data in Sec. V, and finish with a brief discussion and suggestions for future work in Sec. VI.

II. SGWB AND SEARCH METHODS

If we assume the SGWB is isotropic, Gaussian, stationary, and unpolarized, then it is fully characterized by the dimensionless energy density per logarithmic frequency interval

$$\Omega_{\rm gw}(f) = \frac{1}{\rho_c}\frac{{\rm d}\rho_{\rm gw}(f)}{{\rm d}\ln(f)}, \tag{1}$$

where ${\rm d}\rho_{\rm gw}$ is the GW energy density in the frequency interval $\ln f$ to $\ln f + {\rm d}\ln f$, and $\rho_c = 3H_0^2c^2/(8\pi G)$ is the critical energy density to close the Universe. It is common to model the SGWB spectrum as a power law:

$$\Omega_{\rm gw}(f) = \Omega_\alpha\left(\frac{f}{f_{\rm ref}}\right)^\alpha, \tag{2}$$

where Ω_α is the amplitude at a reference frequency, $f_{\rm ref}$, and α is the spectral index. We will use $f_{\rm ref} = 25$ Hz.

Unresolved CBCs give a background spectrum with $\alpha = 2/3$; slow roll inflation models and cosmic strings predict $\alpha = 0$. It is also common to consider a model that is flat in GW power, which corresponds to $\alpha = 3$, to mimic signals like those from phase transitions and supernovae [8]. Recent estimates suggest that the SGWB could be detected by the Advanced LIGO and Advanced Virgo detector network once these detectors reach design sensitivity and integrate for $\mathcal{O}$(years) [7].

In what follows, we consider a SGWB search that uses a cross-correlation estimator that is optimal for a Gaussian, stationary, unpolarized, and isotropic background. Our estimator, $\hat{C}_{ij}(f)$, for the SGWB measured from detectors i and j is

$$\hat{C}_{ij}(f;t) = \frac{2}{T}\frac{{\rm Re}[\tilde{s}_i^*(f;t)\tilde{s}_j(f;t)]}{\Gamma_{ij}(f)S_0(f)}, \tag{3}$$

where $\tilde{s}_i(f;t)$ is the Fourier transform of the strain time series in detector i starting at time t, $\Gamma_{ij}(f)$ is the normalized overlap reduction function (ORF) [13,23] between detectors i and j, T is the duration over which the Fourier transform is taken, and $S_0(f)$ is the spectral shape for a SGWB that is flat in energy density, $S_0(f) = 3H_0^2/(10\pi^2 f^3)$.

In the limit where the total GW strain amplitude in detector i, $\tilde{h}_i(f)$, is much less than the intrinsic detector noise, $\tilde{n}_i(f)$, the variance of $\hat{C}_{ij}(f;t)$ is given by

$$\sigma_{ij}^2(f;t) = \frac{1}{2\Delta f T}\frac{P_i(f;t)P_j(f;t)}{\Gamma_{ij}(f)^2 S_0(f)^2}, \tag{4}$$

where $P_i(f;t)$ is the one-sided power spectral density (PSD) of detector i between times t and $t+T$, and Δf is the frequency resolution.

In general, Eqs. (3) and (4) are estimated for many short time segments of $T = 192$ s and these segments are optimally combined in a postprocessing step given by

$$\hat{C}_{ij}(f) = \frac{\sum_k \hat{C}_{ij,k}(f)\sigma_{ij,k}^{-2}(f)}{\sum_k \sigma_{ij,k}^{-2}(f)}, \tag{5}$$

$$\sigma_{ij}(f) = \left(\sum_k \sigma_{ij,k}^{-2}(f)\right)^{-1/2}, \tag{6}$$

where k indexes the time segments. For a set of N_t time segments starting at times $\{t_k\}_{k=1}^{k=N_t}$, we have defined $\hat{C}_{ij,k}(f) = \hat{C}_{ij}(f;t_k)$, and likewise for its variance.

It is worth considering the expectation value of the estimator, $\langle \hat{C}_{ij}(f) \rangle$, in some detail (we will suppress the time dependence for brevity). Let us assume that $\tilde{s}_i(f)$ can be written as

$$\tilde{s}_i(f) = \tilde{h}_i(f) + \tilde{n}_i(f), \tag{7}$$

where $\tilde{n}_i(f)$ is the Fourier transform of the instrument noise in detector i, and

$$\tilde{h}_i(f) = \sum_A \int \mathrm{d}^2\hat{r} F_i^A(f,\hat{r}) \tilde{h}_A(f,\hat{r}) e^{-2\pi i f \vec{x}_i \cdot \vec{r}/c} \tag{8}$$

is the total GW signal in detector i located at $\vec{x}_i$. Here $F_i^A(f,\hat{r})$ is the response of detector i to a plane wave traveling in direction $\hat{r}$ with polarization A, and $\tilde{h}_A(f,\hat{r})$ is the Fourier amplitude of that plane wave. Consequently,

$$\begin{aligned}\langle \tilde{s}_i^*(f)\tilde{s}_j(f') \rangle = {} & \langle \tilde{h}_i^*(f)\tilde{h}_j(f') \rangle + \langle \tilde{h}_i^*(f)\tilde{n}_j(f') \rangle \\ & + \langle \tilde{n}_i^*(f)\tilde{h}_j(f') \rangle + \langle \tilde{n}_i^*(f)\tilde{n}_j(f') \rangle. \end{aligned} \tag{9}$$

If we assume that the SGWB is isotropic, Gaussian, stationary, and unpolarized, then it is well described by a single power spectral density $S_{\mathrm{gw}}(f)$,

$$\langle \tilde{h}_i^*(f)\tilde{h}_j(f') \rangle = \frac{1}{2}\delta_T(f-f')\Gamma_{ij}(f)S_{\mathrm{gw}}(f), \tag{10}$$

where $\delta_T(f-f')$ is the finite-time approximation to the Dirac delta function, and $S_{\mathrm{gw}}(f)$ is related to the dimensionless energy density as follows:

$$S_{\mathrm{gw}}(f) = \frac{3H_0^2}{10\pi^2}\frac{\Omega_{\mathrm{gw}}(f)}{f^3}. \tag{11}$$

Note that, for the existing detectors, the overlap reduction function, $\Gamma_{ij}(f)$, accounts for all the geometric factors that come into play when cross-correlating data from different detectors [13].

Combining Eqs. (9)–(11), substituting into Eq. (3), and then including the time dependence again, we find

$$\langle \hat{C}_{ij}(f;t) \rangle = \Omega_{\mathrm{gw}}(f) + 2\mathrm{Re}\left[\frac{\langle \tilde{n}_i^*(f;t)\tilde{n}_j(f;t) \rangle}{T\Gamma_{ij}(f)S_0(f)}\right], \tag{12}$$

where we have assumed that the GW signal and the intrinsic noise are uncorrelated, $\langle \tilde{h}_i^*(f)\tilde{n}_j(f') \rangle = 0$, and that the noise in each frequency bin is independent. It is clear from Eq. (12) that in the absence of correlated noise, i.e., $\langle \tilde{n}_i^*(f)\tilde{n}_j(f) \rangle = 0$, $\langle \hat{C}_{ij}(f) \rangle$ is an estimator for $\Omega_{\mathrm{gw}}(f)$. However, this is not the case when $\langle \tilde{n}_i^*(f)\tilde{n}_j(f) \rangle \neq 0$.

Schumann resonances are a potential source of correlated magnetic noise. An estimate of the correlated magnetic noise contribution in the isotropic SGWB search using data from Advanced LIGO's first and second observing runs indicates that it is not yet an issue for current searches [24]. However, as detectors grow more sensitive, this will likely change, and the magnetic noise budget could dominate the signal [16]. Hence, a careful treatment of correlated magnetic noise is of vital importance.

III. SIMULATING GW DATA WITH CORRELATED NOISE

In this section, we discuss how we simulate GW data that is contaminated with correlated noise due to the Schumann resonances. In Sec. III A we discuss the Schumann resonances and their general properties. In Sec. III B we present a model for the coupling of magnetic fields into GW detectors. In Sec. III C we show how to simulate multiple data streams that have correlated Gaussian noise components, and then we apply that method to our specific use case.

A. Schumann resonances

In 1952, Schumann predicted the existence of global extremely low frequency peaks in the electromagnetic field of Earth, which were subsequently observed [25,26]. The resonances are eigenmodes of the conducting spherical cavity formed by the surface of Earth and its ionosphere, and are excited by lightning discharges [27]. The first harmonic, which corresponds to the circumference of Earth, is at hertz, and the subsequent harmonics are at 14, 20.8, and 27.3 Hz. The first mode has the strongest resonance peak, with each consecutive peak being weaker than the previous one. In Fig. 1, we show the power spectral density seen in low-noise magnetometers on site at the Advanced Virgo detector. We can clearly see the first five harmonics of the Schumann resonances. There is a diurnal variation in the amplitude of the Schumann resonances that corresponds to electrical storms that start at similar times and places each day [28,29]. The amplitude of the resonance peaks can vary by as much as a factor of 2 between the loudest and quietest times of the day, depending on the time of year and the location [27,29,30]. What is shown in Fig. 1 represents a trough in the height of the peaks over the course of the day at Virgo. Despite this diurnal variation, we will model the spectrum as stationary in this paper for simplicity.

The Schumann resonances, being global excitations, are coherent across the $\mathcal{O}(1000\ \mathrm{km})$ distance scales between GW detectors [19,20]. We model the time series induced in magnetometers from the Schumann resonances

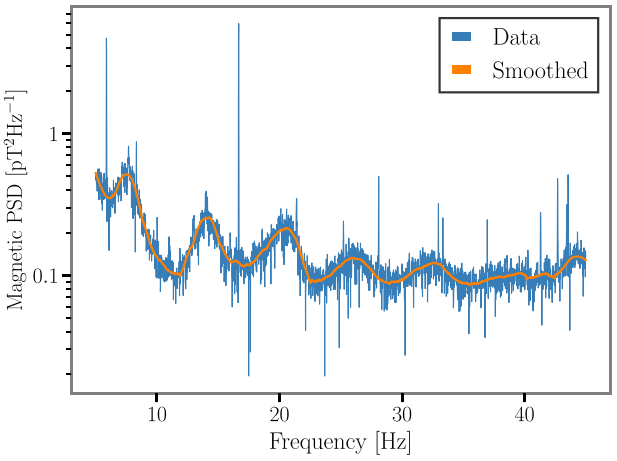

FIG. 1. Power spectral density of magnetometer data near the Advanced Virgo detector. The blue is the inverse-averaged power spectral density for many 32 s chunks of data for the period from 00:00 to 02:00 UTC on July 9, 2019. We use inverse averaging to account for possible magnetic transients that occur during this time. We produce the orange curve by removing the large, narrow spectral features and applying a smoothing filter. We can clearly see five harmonics of the Schumann resonances. The large, narrow spectral features are caused by local magnetic noise on site at Virgo.

as Gaussian, stationary, and unpolarized, with a power spectral density that can be described by a set of Lorentzians centered around the main harmonics. We assume that the data in two magnetometers, $\tilde{m}_i(f)$ and $\tilde{m}_j(f)$, have a cross-spectral density given by

$$\langle \tilde{m}_i^*(f)\tilde{m}_j(f')\rangle = \frac{1}{2}\delta_T(f-f')\gamma_{ij}^M(f)M(f), \quad (13)$$

where $M(f)$ is the correlated power spectral density and $\gamma_{ij}^M(f)$ is the magnetic analog to the GW ORF, Γ_{ij}. This model is equivalent to Eq. (23) of [17], and we refer the reader to that paper for an in-depth discussion of the model.

B. Coupling to detectors

Magnetic fields can induce noise in GW detectors by coupling to metallic materials in the suspension system of the detector, or by inducing currents in the cabling. The magnetic coupling is estimated by injecting magnetic noise into the detector, and measuring the detector's response, and the response of the witness magnetometers near the detectors. Peaks in the detectors' strain channels are related to the peaks in the magnetometer channels via the coupling function, $T(f)$ [15]:

$$\tilde{n}(f) = T(f)\tilde{m}(f). \quad (14)$$

The exact frequency dependence of the coupling function is uncertain, and it can change over the course of a long observation run [31]. Throughout this paper, we will assume that the coupling is constant in time, is well described by a power law, and is real. It takes the form

$$T(f) = \kappa\left(\frac{f}{10\ \text{Hz}}\right)^{-\beta} \times 10^{-23}\ \text{strain/pT}, \quad (15)$$

where κ is the amplitude of the coupling at 10 Hz and β is the spectral index of the power law. In [16], they estimated a coupling function with $\kappa = 2$, $\beta = 2.67$ for LIGO Hanford Observatory (LHO). Measurements made after the second observation run (O2) found $\kappa = 0.38$ at LHO and $\kappa = 0.25$ at LIGO Livingston Observatory (LLO), and $\beta = 3.55$, 4.61 [31] at LHO and LLO, respectively. Meanwhile for Virgo, post-O2 measurements indicate $\kappa = 0.275$ and $\beta = 2.50$ [32]. These measurements highlight that the coupling functions differ in both shape and amplitude at each site.

We made three simplifying assumptions in defining Eq. (15), and relaxing each of these assumptions will need to be explored further in future work. For example, it is known that the strength of the coupling function can change as a function of time due to things like routine maintenance on the detectors. Next, recent measurements at LHO indicate that $T(f)$ has a more complicated frequency structure than a simple power law. There is evidence, for example, of a shift to a positive spectral index near 60 Hz. Finally, the assumption that $T(f)$ is real will also need to be revisited in the future. It could be modeled by multiplying Eq. (15) by a frequency-dependent phasor term, $e^{i\phi(f)}$, but there are no measurements at present for the frequency structure of that phase or how it behaves as a function of time. It is possible to generalize the simulations we perform to inject signals that relax these assumptions and evaluate the effect they have on the method we discuss later; however, we reserve such studies for future work.

C. Simulating data

In this section, we first discuss how we generate correlated synthetic magnetometer data streams with a specific overlap reduction function and cross power. We then discuss how we translate that into strain data using a coupling function. We close with a discussion of the parameters we use to simulate the data.

1. Simulating correlated Gaussian signals

Here we discuss simulating a correlated Gaussian signal with a specific $M(f)$ and $\gamma_{ij}^M(f)$ between detectors. Let us consider a network of N detectors. Individual on-site magnetometer measurements combine to give an N-dimensional column vector, $\tilde{\boldsymbol{m}}(f)$, and the magnetic

overlap reduction functions are then a Hermitian $N \times N$ matrix, $\boldsymbol{\gamma}^M(f)$:

$$\langle \tilde{\boldsymbol{m}}(f)\tilde{\boldsymbol{m}}^\dagger(f')\rangle = \frac{1}{2}\delta(f-f')\boldsymbol{\gamma}^M(f)M(f). \tag{16}$$

The individual elements of the $\boldsymbol{\gamma}^M(f)$ matrix represent the overlap reduction function between different baselines, evaluated at f. We then decompose $\boldsymbol{\gamma}^M$ using a Cholesky decomposition [33]:

$$\boldsymbol{\gamma}^M(f) = \boldsymbol{L}(f)\boldsymbol{L}(f)^\dagger, \tag{17}$$

where $\boldsymbol{L}(f)$ is a lower-triangular matrix. We can then use $\boldsymbol{L}(f)$ to construct the correlated magnetometer data,

$$\tilde{\boldsymbol{m}}(f) = \sqrt{\frac{M(f)}{2}}\boldsymbol{L}(f)\tilde{\boldsymbol{\eta}}(f), \tag{18}$$

with $\tilde{\boldsymbol{\eta}}(f)$ being white Gaussian noise with a covariance matrix given by the identity matrix:

$$\langle \tilde{\boldsymbol{\eta}}(f)\tilde{\boldsymbol{\eta}}^\dagger(f')\rangle = \boldsymbol{I}\delta(f-f'). \tag{19}$$

Once we obtain $\tilde{\boldsymbol{m}}(f)$, which mimic local magnetometer measurements, we project it onto the detectors using a power-law coupling function as in Eq. (15). We then inverse-Fourier transform that strain spectrum to produce $\boldsymbol{h}(t)$, and add it to Gaussian detector noise that is uncorrelated between the separate detectors and has a PSD consistent with design sensitivity for the Advanced LIGO and Advanced Virgo detectors [34].

2. Correlated magnetic noise PSD and $\gamma^M_{ij}(f)$ for synthetic datasets

When constructing a dataset with synthetic magnetic noise, we must choose a power spectral density of the correlated magnetic signal between sites, $M(f)$. This PSD should include the first several harmonics of the Schumann resonances. Throughout the rest of this paper, we model each peak as a separate Lorentzian, with the fundamental peak having an amplitude of 1 $\mathrm{pT}^2/\mathrm{Hz}$. A plot of the simulated PSD is shown in Fig. 2. We only include harmonics below 30 Hz for this study. While the true correlated magnetic PSD does not fall off as rapidly as our simulated version, the steep coupling functions we consider in Sec. V will make higher frequencies negligible when the magnetic noise is projected onto the detectors.

We use the real part of coherence measurements between magnetometers located on site at LHO, LLO, and Virgo to estimate $\gamma^M_{ij}(f)$ for each detector pair, and we use these measurements throughout the rest of this paper when creating synthetic datasets. Our use of the real part of the coherences in this case does not affect the results. This can be seen by substituting Eq. (14) into Eq. (12). A term like Eq. (13) comes out, multiplied by $T_i(f)$ and $T_j(f)$, which are assumed to be real. A similar, explicit calculation along these lines is done in Sec. IV. If $T_i(f)$ were not real, then we would need to use the full, complex coherences for $\gamma^M_{ij}(f)$. More details related to these measurements are discussed in the Appendix. A plot of the measured $\gamma^M_{ij}(f)$ is shown for the three detector pairs of interest in Fig. 3. For comparison, we also include $\Gamma_{ij}(f)$, which is the analogous quantity for GWs. The differences between $\gamma^M_{ij}(f)$ and $\Gamma_{ij}(f)$ help us to discriminate between correlated magnetic noise and a SGWB in Sec. IV.

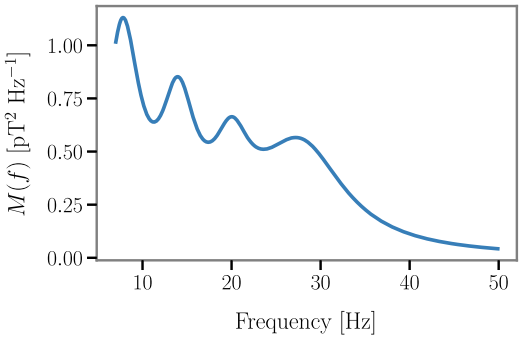

FIG. 2. Injected $M(f)$ spectrum. We simulate the first four Schumann peaks as Lorentzians with reasonable amplitudes and widths.

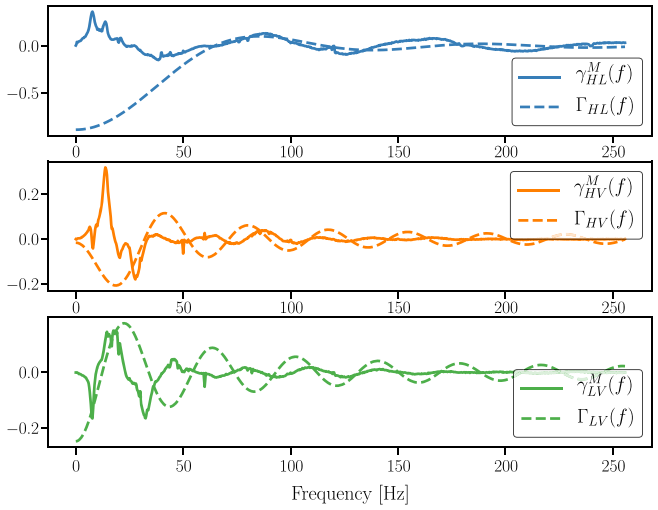

FIG. 3. From top to bottom we show $\gamma^M_{ij}(f)$ (solid lines) and $\Gamma_{ij}(f)$ (dashed lines) for $ij = \mathrm{HL}$, HV, and LV. We discuss how we measure $\gamma^M_{ij}(f)$ in the Appendix.

IV. SIMULTANEOUS ESTIMATION OF CORRELATED NOISE AND GRAVITATIONAL WAVES

Various techniques have been proposed to address correlated noise due to Schumann resonances in the output of GW detectors. The most prominent of these techniques is Wiener filtering [15,16,19,20]. Wiener filtering relies on witness magnetometers that are positioned near the detectors in order to experience the same Schumann resonances, but not too close to be exposed to the local magnetic noise. The downside of Wiener filtering is that it requires a large coherence between the witness and target channels, which means that for weakly coupled signals it can be difficult to completely subtract the noise [19,20].

We propose an alternative method to address correlated noise, specifically as it pertains to a search for a SGWB. We model the correlated magnetic noise in GW detectors using the data collected by the magnetometers placed near the detector sites, and a parametrized model for the magnetic field to GW detector coupling. We then include this model as a contribution to the estimator, $\hat{C}_{ij}(f)$ in Eq. (3), together with a SGWB model. The way we treat magnetometer data here is reminiscent of the *a priori* subtraction scheme presented in [16], except that here we offer a straightforward way to handle uncertainty in the measurement of the coupling functions by treating them as nuisance parameters that we marginalize over. We reserve a comparison between our method and Wiener filtering for future work.

A. Correlated noise model

We can rewrite Eq. (11) to include separate correlated magnetic and uncorrelated noise terms

$$\tilde{s}_i(f) = \tilde{h}_i(f) + \tilde{n}_i^{\mathrm{u}}(f) + T_i(f)\tilde{m}_i(f), \tag{20}$$

where $\tilde{n}_i^{\mathrm{u}}(f)$ is the uncorrelated noise in detector i, and $T_i(f)\tilde{m}_i(f)$ represents the correlated magnetic noise. Substituting Eqs. (20) and (15) into Eq. (3) we find

$$\langle \hat{C}_{ij}(f) \rangle = \Omega_{\mathrm{gw}}(f) + \Omega_{\mathrm{M},ij}(f), \tag{21}$$

where $\Omega_{\mathrm{M},ij}(f)$ represents the magnetic contribution, which we derive next.

We construct the magnetic model, $\Omega_{M,ij}(f)$, by first treating local magnetometer data the same way we analyze GW strain data. We break the magnetometer data into $T = 192$ s data chunks, and we calculate the cross-power term in the same way as Eq. (3), replacing the strain data with local magnetometer data. That is, for the data between t_k and $t_k + T$ we calculate

$$\hat{M}_{ij,k}(f) = \frac{2}{T}\frac{\mathrm{Re}[\tilde{m}_i^*(f;t_k)\tilde{m}_j(f;t_k)]}{\Gamma_{ij}(f)S_0(f)}. \tag{22}$$

We postprocess the magnetometer data with the same weights used for postprocessing the GW data, viz.

$$\hat{M}_{ij}(f) = \frac{\sum_k \hat{M}_{ij,k}(f)\sigma_{ij,k}^{-2}(f)}{\sum_k \sigma_{ij,k}^{-2}(f)}. \tag{23}$$

The weights, $\sigma_{ij,k}(f)$, are the same as those expressed in Eq. (4). They are calculated using *GW strain data* and not magnetometer data. This way we treat the magnetometer data the same way the magnetic contribution to the final $\hat{C}_{ij}(f)$ statistic is treated. We then use this final measurement to construct the magnetic contribution to the model, which is given by

$$\Omega_{\mathrm{M},ij}(f) = \kappa_i\kappa_j\left(\frac{f}{10\ \mathrm{Hz}}\right)^{-\beta_i-\beta_j}\hat{M}_{ij}(f) \times 10^{-22}. \tag{24}$$

The factor of 10^{-22} assumes that the units of $\tilde{m}_i(f)$ are $\mathrm{T\,Hz^{-1}}$.

B. Parameter estimation and model selection

We use a parameter estimation and model selection scheme similar to those set out in [10,11,35]. We choose a Gaussian likelihood for $\hat{C}_{ij}(f)$ given by

$$\ln p(\hat{C}_{ij}(f)|\boldsymbol{\theta}_{\mathrm{gw}}, \boldsymbol{\theta}_{\mathrm{M}}) = -\frac{1}{2}\sum_f \left\{ \frac{[\hat{C}_{ij}(f) - \Omega_{\mathrm{gw}}(f, \boldsymbol{\theta}_{\mathrm{gw}}) - \Omega_{\mathrm{M},ij}(f, \boldsymbol{\theta}_{\mathrm{M}})]^2}{\sigma_{ij}^2(f)} + \ln\left(2\pi\sigma_{ij}^2(f)\right) \right\}, \tag{25}$$

where $\boldsymbol{\theta}_{\mathrm{gw}}$ and $\boldsymbol{\theta}_{\mathrm{M}}$ represent parameters for the GW and magnetic models, respectively. In the case where we have cross-correlation statistics for multiple baselines, we consider the total likelihood to be the product of the individual likelihoods for each pair of detectors. The resulting multi-baseline likelihood is given by

$$p(\{\hat{C}_{ij}(f)\}_{ij\in\mathrm{pairs}}|\boldsymbol{\theta}_{\mathrm{gw}}, \boldsymbol{\theta}_{\mathrm{M}}) = \prod_{ij\in\mathrm{pairs}} p(\hat{C}_{ij}(f)|\boldsymbol{\theta}_{\mathrm{gw}}, \boldsymbol{\theta}_{\mathrm{M}}). \tag{26}$$

It is straightforward to use Eq. (26) to estimate the posterior distribution of the parameters, $\boldsymbol{\theta}_{\mathrm{gw}}$ and $\boldsymbol{\theta}_{\mathrm{M}}$, either

TABLE I. List of prior distributions used for each parameter for results presented in Secs. V B 1 and V B 2.

Parameter	Prior
$\Omega_{2/3}$	LogUniform(10^{-12}, 10^{-7})
κ_H	Uniform(0, 10)
κ_L	Uniform(0, 10)
κ_V	Uniform(0, 10)
β_H	Uniform(0, 10)
β_L	Uniform(0, 10)
β_V	Uniform(0, 10)

by brute-force calculation or by Markov chain Monte Carlo methods [36,37].

We will also compare different models for the data using Bayesian model selection. The four models we consider are

(1) **NOISE**: $\Omega_{\rm M}(f) = \Omega_{\rm gw}(f) = 0$,
(2) **GW**: $\Omega_{\rm M}(f) = 0$, $\Omega_{\rm gw}(f) \neq 0$,
(3) **SCHU**: $\Omega_{\rm M}(f) \neq 0$, $\Omega_{\rm gw}(f) = 0$,
(4) **GW+SCHU**: $\Omega_{\rm M}(f) \neq 0$, $\Omega_{\rm gw}(f) \neq 0$.

The form of the SGWB model, $\Omega_{\rm gw}(f)$, is the power law in Eq. (2), with $\boldsymbol{\theta}_{\rm gw} = \Omega_{2/3}$ and $\alpha = 2/3$ fixed. The form of $\Omega_{\rm M}(f)$ is given by Eq. (24) with $\boldsymbol{\theta}_{\rm M} = (\kappa_i, \kappa_j, \beta_i, \beta_j)$ when two detectors are involved. Another set of coupling parameters are included when a third detector is used.

We compare these models using Bayes factors [38]. For example, comparing the **GW** model to the **NOISE** model we have

$$\mathcal{B}^{\rm GW}_{\rm NOISE} = \frac{\int {\rm d}\boldsymbol{\theta}_{\rm gw} p(\hat{C}_{ij}(f)|\boldsymbol{\theta}_{\rm gw}) p(\boldsymbol{\theta}_{\rm gw})}{\mathcal{N}}, \qquad (27)$$

where $\mathcal{N}$ is given by evaluating Eq. (25) for $\Omega_{\rm M}(f) = \Omega_{\rm gw}(f) = 0$, and $p(\boldsymbol{\theta}_{\rm gw})$ is the prior on the GW model parameters. When $\mathcal{B}^{\rm GW}_{\rm NOISE} > 1$ there is support for the **GW** model compared to the **NOISE** model. A further discussion of interpretation of Bayes factors can be found in, e.g., Chap. 3 of [14]. In this paper, we will consider "strong" support for one model over another when $\ln \mathcal{B} > 8$. The numerator of Eq. (27) is referred to as the evidence of the **GW** model and is denoted $\mathcal{Z}_{\rm GW}$. The prior distribution used for each parameter in the model throughout the rest of this paper is shown in Table I.

We use the nested sampler CPNest [38,39] through the front-end package BILBY [40] to both explore the posterior distribution of each parameter and estimate the evidence for each model.

V. RESULTS ON SYNTHETIC DATA

In this section we show results for end-to-end simulations of a SGWB search using GW data with correlated magnetic noise. In Sec. V A we briefly review data simulation schemes in the time and frequency domains.

TABLE II. Correlated magnetic noise parameters for four different synthetic datasets.

Run name	$\kappa_{\rm H}$	$\beta_{\rm H}$	$\kappa_{\rm L}$	$\beta_{\rm L}$	$\kappa_{\rm V}$	$\beta_{\rm V}$
None	0	0	0	0	0	0
Realistic	0.38	3.55	0.35	4.61	0.275	2.50
Strong	5	3.55	5	4.61	5	2.50

In the rest of this section we seek to answer three main questions:

(1) How does including three detectors aid in our ability to detect the correlated magnetic noise and constrain parameters associated with it?
(2) Can we detect GWs in the context of correlated magnetic noise? How is the significance of the detection affected by the presence of that noise?
(3) Can a noisy measurement of $\hat{M}_{ij}(f)$ or a strong correlated magnetic signal lead to a false SGWB detection?

A. Synthetic data and parameters

1. Time series simulations

We simulate the strain time series for the LHO, LLO, and Virgo detectors with correlated magnetic noise using the techniques described in Sec. III. We then run the standard pipeline used by LIGO-Virgo for the isotropic search for a SGWB to calculate $\hat{C}_{ij}(f)$ and $\hat{M}_{ij}(f)$ for all possible detector pairs.[1] All SGWB injections are made in the frequency domain on those data products and assume a power-law spectrum with $\alpha = 2/3$ to mimic an astrophysical SGWB from unresolved CBCs.

The three different year-long synthetic datasets we consider are described in Table II. We consider datasets with no correlated magnetic noise (**none**), realistic correlated magnetic noise (**realistic**) based on post-O2 measurements [31,32], and strong correlated magnetic noise (**strong**). The **strong** dataset corresponds to a larger coupling strength than we currently observe, but is meant to be a stand-in for situations where we do observe correlated magnetic noise. This could occur either due to an increase in the sensitivity of detectors or a change in the coupling functions themselves.

2. Frequency-domain simulations

For Monte Carlo simulations of many noise realizations we will directly simulate Eq. (24) in the frequency domain. This simulation method is used in the final two parts of this section, and will also consider the same **none**, **realistic**, and **strong** scenarios detailed in Table II.

[1]See https://git.ligo.org/stochastic-public/stochastic.

B. Advantages in detecting correlated magnetic noise using a three-detector network

We begin by looking at the advantage of having a three-detector, global network as opposed to a simple two-detector network. To evaluate this situation, we use the time-domain data discussed previously. We first look at the effect using three detectors has on model selection, before discussing the advantages of using three detectors when performing parameter estimation.

1. Model selection

In Table III we show log-Bayes factors comparing different models when there is no injected SGWB. The first column indicates the strength of the correlated noise injection and the second column indicates which detectors were used in the parameter estimation. The other four columns present Bayes factors comparing different models.

The results for the **none** and **realistic** injections are shown in the first four rows of Table III. The log-Bayes factors indicate that there is no preference for a model with correlated magnetic noise compared to Gaussian noise ($\ln \mathcal{B}^{\mathrm{SCHU}}_{\mathrm{NOISE}}$) or for any model that includes a SGWB compared to Gaussian noise ($\ln \mathcal{B}^{\mathrm{GW}}_{\mathrm{NOISE}}$ and $\ln \mathcal{B}^{\mathrm{SCHU+GW}}_{\mathrm{NOISE}}$). Thus, insofar as our simple coupling model is accurate, it is unlikely that at design sensitivity Schumann resonances will be detectable after one year of integration time. However, the coupling functions can change as a function of time, and how they impact the search is highly sensitive to the strength and frequency spectrum of the coupling between the magnetic field and the strain channel of the detector.

The **strong** injection results are shown in the fifth and sixth rows of Table III. There is little evidence for correlated magnetic noise with the Hanford-Livingston pair of detectors, but when we include Virgo in the network, we make a clear detection, with $\ln \mathcal{B}^{\mathrm{SCHU}}_{\mathrm{NOISE}} = 33.29$. While we make a detection of Schumann resonances, $\ln \mathcal{B}^{\mathrm{SCHU+GW}}_{\mathrm{SCHU}} = 0.38$ indicates that there is no preference for a model that also includes a SGWB compared to a model that contains just correlated magnetic noise. Including a third detector significantly aids in our ability to detect and characterize correlated magnetic noise in this situation.

TABLE III. We show odds ratios that compare different models when no GW injection is made. We show results for all three injected datasets using just the Hanford (H), Livingston (L) pair, as well as the full Hanford, Livingston, Virgo (V) network.

Run name	Dets	$\ln \mathcal{B}^{\mathrm{GW}}_{\mathrm{NOISE}}$	$\ln \mathcal{B}^{\mathrm{SCHU}}_{\mathrm{NOISE}}$	$\ln \mathcal{B}^{\mathrm{SCHU+GW}}_{\mathrm{NOISE}}$	$\ln \mathcal{B}^{\mathrm{SCHU+GW}}_{\mathrm{SCHU}}$
None	HL	−0.65	−0.26	−1.0	−0.74
None	HLV	−0.75	0.45	−0.32	−0.77
Realistic	HL	−0.61	−0.36	−1.01	−0.65
Realistic	HLV	−0.57	−0.53	−1.18	−0.65
Strong	HL	0.28	0.32	0.59	0.27
Strong	HLV	0.59	33.29	33.67	0.38

2. Parameter estimation

It is also important that we are able to accurately recover the correct parameters for the SGWB, even when there is a strong correlated magnetic noise injection.

In Fig. 4, we show a corner plot with 1D and 2D marginalized posterior distributions for each parameter over which we sample for the **strong** injection (last row of Table II). In this case, there is no SGWB. The green posteriors indicate using only LHO and LLO, while the blue include Virgo in the network as well. It is clear that including Virgo significantly improves our estimates of the Schumann parameters. In the two-detector scenario the magnetic parameters are nearly unconstrained. Whereas, when using the three-detector network, we are able to achieve reasonable estimates of β_H, β_L, and β_V. This makes sense given the model selection results (fifth and sixth rows of Table III), which indicate that adding Virgo improved our ability to detect correlated magnetic noise. Furthermore, the posterior on $\Omega_{2/3}$ in Fig. 4 can be used to set an upper limit on $\Omega_{2/3}$ in the presence of correlated magnetic noise. In Sec. V C, where we perform frequency-domain injections, we will discuss how upper limits on $\Omega_{2/3}$ are affected by the presence of correlated magnetic noise.

In Fig. 5 we show posteriors with a SGWB injection of $\Omega_{2/3} = 10^{-8}$. The strength of this injection is chosen for illustrative purposes. We see that the posterior on $\Omega_{2/3}$ is well constrained but represents an overestimate of the true injected value by 14%. Due to computational restrictions, we are unable to perform repeated time-domain simulations to evaluate whether this is a systematic bias in our method. However, we did perform repeated frequency-domain simulations (using the method described in Sec. V A 2) with magnetic and gravitational-wave parameters drawn from the priors in Table I. Using probability-probability estimates as a diagnostic [41], we see no evidence of systematic bias on our estimate of $\Omega_{2/3}$.

Including Virgo does not improve our ability to constrain $\Omega_{2/3}$. However, it adds significantly to our ability to detect and constrain parameters in the correlated magnetic noise model. A correlated noise detection that is dominated by pairs of detectors that include Virgo is still able to constrain the coupling function parameters in all three detectors, which means that a third detector can aid in our ability to model the correlated noise contribution in the detector pair that is most sensitive to a SGWB.

C. SGWB detection with correlated magnetic noise

In this section we show we are able to detect GWs when correlated magnetic noise is present and we show

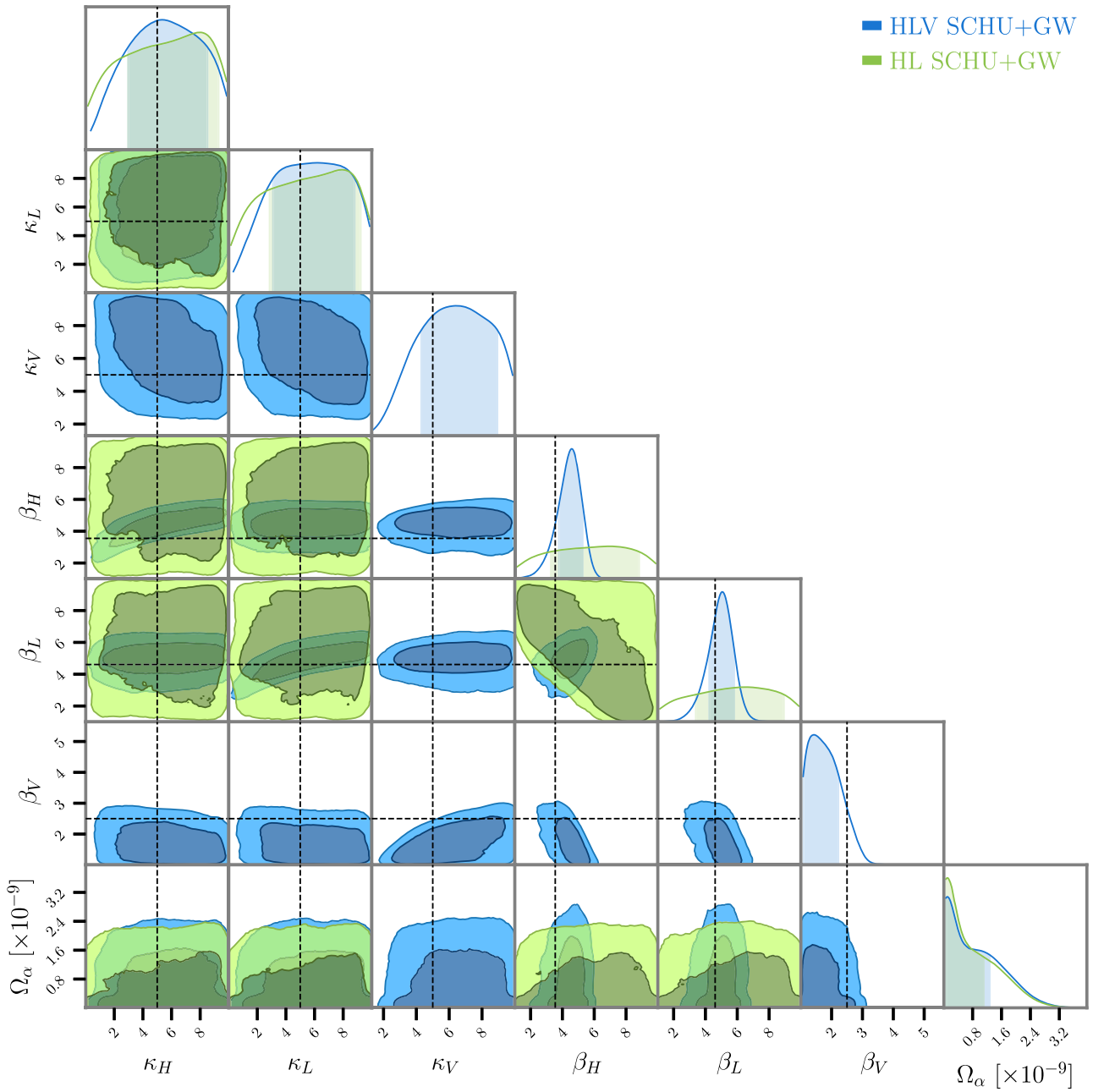

FIG. 4. Parameter estimation results for strong correlated noise injection and no SGWB injection. Blue lines and contours correspond to using Hanford, Livingston, and Virgo data. Green lines and contours correspond to using only the Hanford, Livingston pair of detectors. Dashed lines indicate the injected value of each parameter. It is evident that including three detectors improves the recovery of κ and β for all three detectors. In both cases, the posterior on $\Omega_{2/3}$ is consistent with no SGWB.

how the presence of correlated magnetic noise affects the significance of that detection. We performed 300 Monte Carlo simulations, in the frequency domain, of the **strong** and **none** correlated noise parameters in Table II. We did this for $\Omega_{2/3} = 0, 10^{-8}$, and 3×10^{-9}, assuming 1 yr of integration time. The results are shown in three panels in Fig. 6, where we show the distribution of $\ln \mathcal{B}^{\mathrm{SCHU+GW}}_{\mathrm{SCHU}}$ for each simulation. Throughout this section we use the full three-detector network and all inference is done with the prior distributions in Table I.

The top panel of Fig. 6, where $\Omega_{2/3} = 0$, shows that for both the strong correlated magnetic noise injection (blue, solid) and the no correlated magnetic noise case we see no preference for the model including GWs compared to the one that only includes correlated magnetic noise, as one would expect. In the absence of a detection of $\Omega_{2/3}$, we can

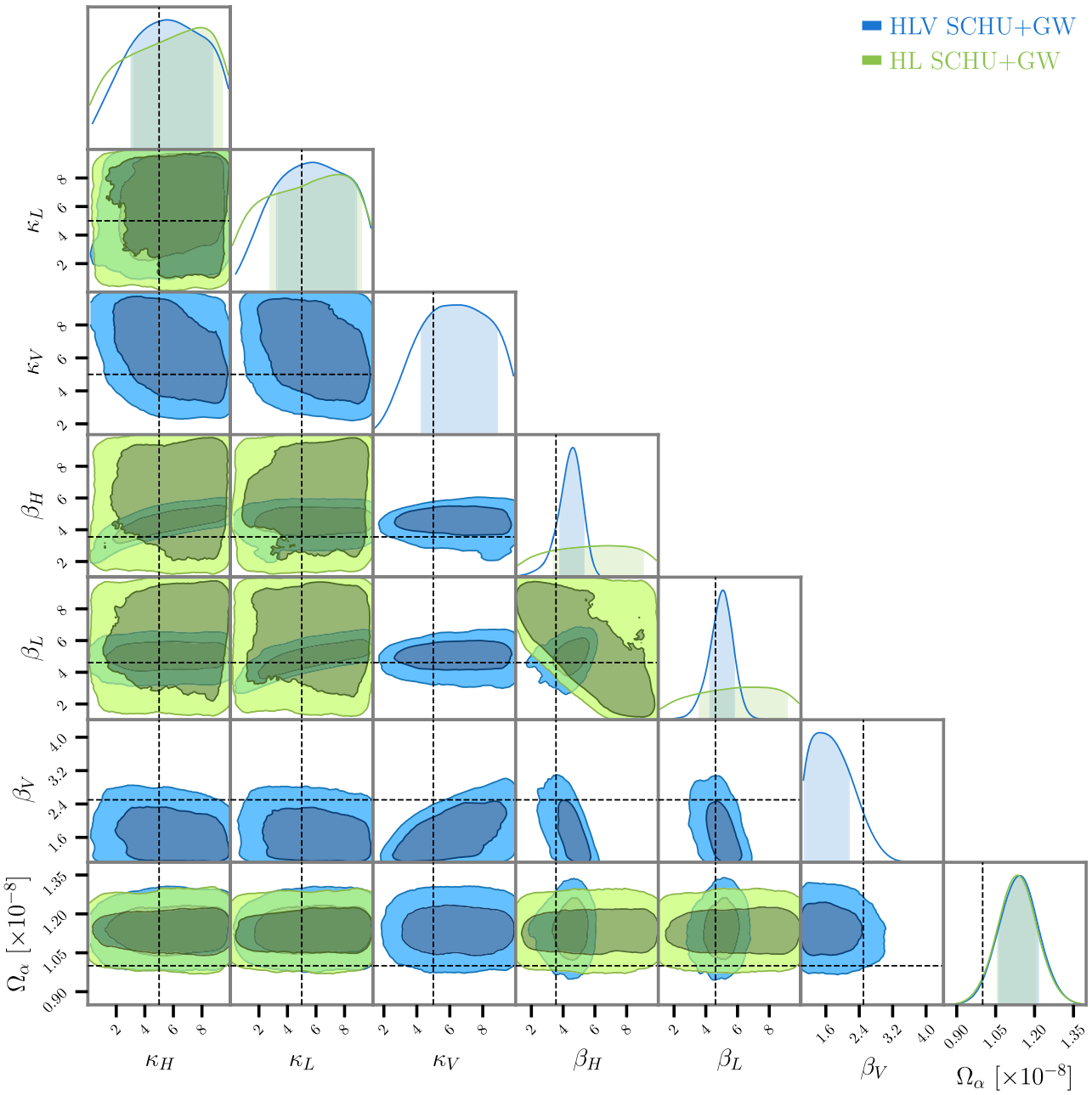

FIG. 5. Parameter estimation results for strong correlated noise injection and $\Omega_{2/3} = 10^{-8}$. Blue lines and contours correspond to using Hanford, Livingston, and Virgo data. Green lines and contours correspond to using only the Hanford, Livingston pair of detectors. Dashed lines indicate the injected value of each parameter. It is evident that including three detectors improves the recovery of κ and β for all three detectors. The posterior distributions of $\Omega_{2/3}$ for both scenarios are consistent with one another, and indicate a 14% overestimate of $\Omega_{2/3}$.

use the posterior distribution on that parameter to set 90% upper limits for each of the 300 realizations. The median 90% upper limit on $\Omega_{2/3}$ set for the ensemble of injections is 4.8×10^{-10} for both the **strong** and **none** cases.

In the middle panel of Fig. 6 we show results for $\Omega_{2/3} = 3 \times 10^{-9}$, which is within the range of the expected SGWB due to unresolved CBCs [7]. There is mild evidence for a SGWB for both distributions, with the **none** distribution (orange, dashed line) peaking at $\ln \mathcal{B}^{\mathrm{SCHU+GW}}_{\mathrm{SCHU}} \approx 6$ and the **strong** distribution (blue, solid line) peaking at $\ln \mathcal{B}^{\mathrm{SCHU+GW}}_{\mathrm{SCHU}} \approx 4$. It is clear that when strong correlated noise is present the significance is lower than when there is no correlated noise.

In the bottom panel of Fig. 6 we show results for $\Omega_{2/3} = 10^{-8}$. This value is larger than expected for an astrophysical background from unresolved CBCs [7], but is

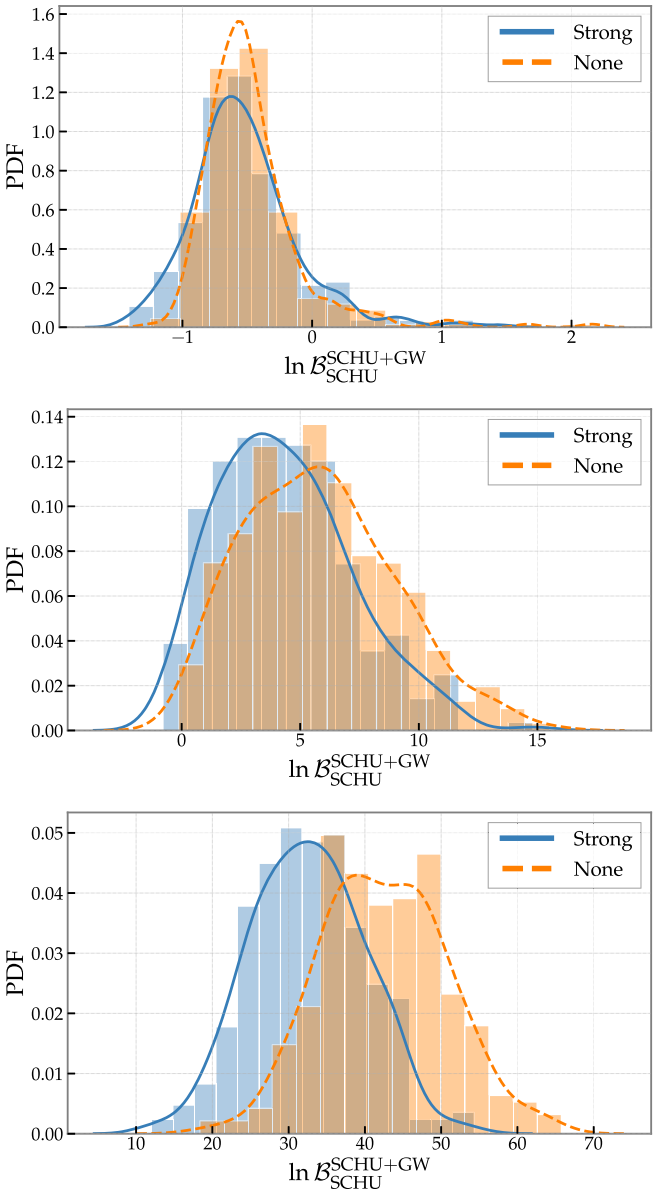

FIG. 6. We show the distribution of $\ln \mathcal{B}^{\mathrm{SCHU+GW}}_{\mathrm{SCHU}}$ for the **strong** (blue, solid) and **none** (orange, dashed) injection parameters, and $\Omega_{2/3} = 0$ (top panel), $\Omega_{2/3} = 3 \times 10^{-9}$ (middle panel), and $\Omega_{2/3} = 10^{-8}$ (bottom panel). In the top panel we see no evidence for a GW detection. In the middle and bottom panels we see evidence the presence of a SGWB in both cases (although that evidence is marginal in the middle panel). The presence of correlated magnetic noise has clearly shifted the Bayes factor distributions downward.

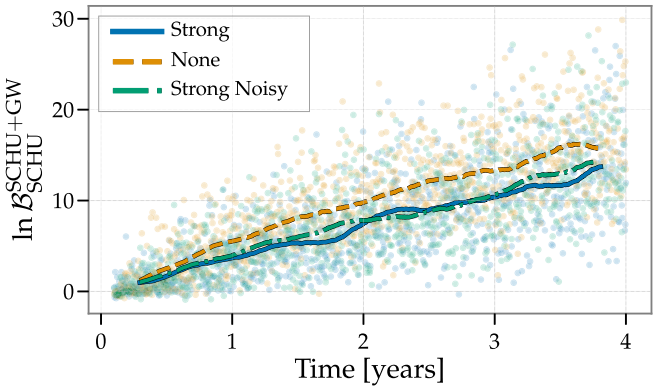

FIG. 7. We show how $\ln \mathcal{B}^{\mathrm{SCHU+GW}}_{\mathrm{SCHU}}$ scales as a function of time using 1000 injections in the frequency domain with increasing observation time with a SGWB injection of $\Omega_{2/3} = 3 \times 10^{-9}$. The **strong** case (blue, solid line) is clearly below the **none** case (orange, dashed line). We also show the **strong** case with a noisy measurement of $\hat{M}_{ij}(f)$ with a magnetic SNR of 5 (green, dash-dotted line). It does not appear that a noisy measurement of $\hat{M}_{ij}(f)$ significantly hinders our ability to detect a SGWB.

chosen for illustrative purposes. When there is strong correlated magnetic noise present (blue, solid line) the distribution peaks at a lower value than when there is no correlated magnetic noise injected (orange, dashed line), indicating a drop in the significance of the SGWB detection when correlated magnetic noise is present. The median of the simulations with **strong** correlated magnetic noise is $\ln \mathcal{B}^{\mathrm{SCHU+GW}}_{\mathrm{SCHU}} = 32.2$ compared to $\ln \mathcal{B}^{\mathrm{SCHU+GW}}_{\mathrm{SCHU}} = 42.2$ for the **none** simulation, corresponding to a 31% drop in the detection statistic.

Figure 6 shows that the presence of correlated magnetic noise reduces the significance of a GW detection. In Fig. 7 we show how $\ln \mathcal{B}^{\mathrm{SCHU+GW}}_{\mathrm{SCHU}}$ scales with time for the **strong** (blue, solid line) and **none** (orange dashed line) cases with an injection of $\Omega_{2/3} = 3 \times 10^{-9}$. We also show a third case where we consider a noisy measurement of $\hat{M}_{ij}(f)$, which we will discuss in Sec. V D. The **strong** and **none** cases are clearly different, and the time to detection (in this case the time to reach $\ln \mathcal{B}^{\mathrm{SCHU+GW}}_{\mathrm{SCHU}} = 8$) is increased to $2.1^{+1.7}_{-0.7}$ yr for the **strong** case compared to $1.5^{+0.9}_{-0.6}$ yr for the **none** case (values given define the 68% confidence regions).

D. Can a poor measurement of $\hat{M}_{ij}(f)$ lead to a false SGWB detection?

To this point, we have not considered the effect of local magnetometer noise, which can reduce the significance with which we measure the noise that is correlated between the detectors. In this section, we address whether a low-SNR measurement of $\hat{M}_{ij}(f)$, defined in Eq. (23), or very strong correlated noise could lead to a false GW detection. To evaluate this question, we perform frequency-domain injections with increasing values of κ from 0 to 9 for each detector, and the same β values for LHO, LLO, and Virgo that were used for the **realistic** and **strong** injections in Table II. For this test, we use the full three-detector network and we extend the upper range of the priors, shown in Table I, on κ from 10 to 20.

We also vary the confidence with which we measure $\hat{M}_{ij}(f)$. We perform our frequency-domain injection using

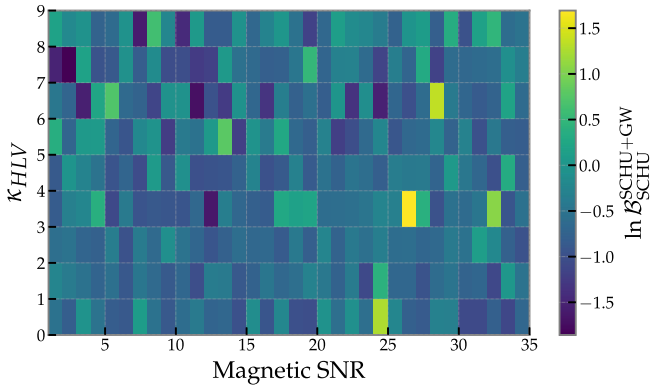

FIG. 8. We show a grid of $\ln \mathcal{B}^{\mathrm{SCHU+GW}}_{\mathrm{SCHU}}$ for different values of κ (the same κ is used for all three detectors) and the magnetic SNR defined in Eq. (28). The range of $\ln \mathcal{B}^{\mathrm{SCHU+GW}}_{\mathrm{SCHU}}$ across the whole grid is consistent with no SGWB detection. This indicates it is unlikely that a false SGWB detection could be caused by a noisy measurement of $\hat{M}_{ij}(f)$ or the presence of strong correlated magnetic noise.

$M(f)$ presented in Fig. 2. We then simulate a "measurement" at a chosen signal-to-noise ratio (SNR) in each frequency bin by drawing $\hat{M}_{ij}(f)$ from a normal distribution with mean $\gamma^M_{ij}(f)M(f)$ and variance $\sigma^2_M(f)$. Due to the fact that the SNR and $M(f)$ are chosen *a priori*, we rearrange the definition of the SNR to set the standard deviation in each frequency bin,

$$\sigma_M(f) = \frac{\gamma^M_{ij}(f)M(f)}{\mathrm{SNR}}. \tag{28}$$

We perform frequency domain injections with SNRs ranging from 1 to 35.

In Fig. 8 we show $\ln \mathcal{B}^{\mathrm{SCHU+GW}}_{\mathrm{SCHU}}$ for the range of κ and magnetic SNR values we inject and with $\Omega_{2/3} = 0$. The Bayes factors in Fig. 8 are consistent with no detection—they span a similar range to those in the top panel of Fig. 6, where we assumed a perfect measurement of $\hat{M}_{ij}(f)$. This result indicates that a false detection of a SGWB is unlikely, even with an uncertain measurement of the Schumann resonances.

We also test whether a noisy measurement of $\hat{M}_{ij}(f)$ could increase time to detection of a SGWB. We do this by showing how $\ln \mathcal{B}^{\mathrm{SCHU+GW}}_{\mathrm{SCHU}}$ scales with time for $\kappa = 5$ (**strong** case) and SNR $= 5$ in Fig. 7 with the green dash-dotted curve. There is a not a clear reduction in detection strength compared to the blue solid curve, which is the same correlated magnetic noise strength but with a no-noise measurement of $\hat{M}_{ij}(f)$. The time to detection for the noisy measurement case is $2.1^{+1.2}_{-0.9}$ yr, which is around 50% longer than the case with no correlated noise and comparable to the case where we make a noiseless measurement of the magnetic field.

VI. DISCUSSION

In this paper we perform realistic simulations of correlated magnetic noise in interferometric gravitational-wave detectors, and propose a new method to detect a SGWB in the presence of that correlated magnetic noise. The method reliably separates a SGWB from correlated magnetic noise, although significance of that detection can be reduced either by the presence of strong correlated noise, or through a noisy measurement of the correlated magnetic fields. We also showed that a three-detector network improves our ability to detect, estimate, and subtract the correlated magnetic noise compared to just a single detector pair. Moreover, in the absence of a SGWB detection, upper limits on the SGWB are a natural by-product of the analysis.

The method presented here is an alternative to Wiener filtering, but could also be used in tandem with Wiener filtering. For example, this method could be used to find correlated noise not successfully subtracted using Wiener filtering. A full comparison of the efficiency of this method compared to Wiener filtering is reserved for future work. Moreover, any proposed SGWB signal could be verified using the geodesy methods discussed in Ref. [21]. In that scenario, the maximum *a posteriori* parameters could be used to subtract off the correlated magnetic noise, and the proposed remaining SGWB signal could be analyzed using geodesy.

This method is easily applicable to current searches for a SGWB, and should help make a reliable detection of a SGWB using ground-based interferometric detectors. Future work should focus on using a model for the magnetic coupling functions that is more flexible than a simple power law, making direct comparisons with other proposed methods, and working toward incorporating the time variability of both coupling functions and Schumann resonances.

ACKNOWLEDGMENTS

The authors would like to thank Thomas Callister, Giancarlo Cella, and the LIGO/Virgo Stochastic Background group for helpful comments and discussions. The authors would also like to thank the scientists on site at the Virgo and LIGO detectors for installation and maintenance of the low-noise magnetometers whose data we used in this paper. Parts of this research were conducted by the Australian Research Council Centre of Excellence for Gravitational Wave Discovery (OzGrav), through Project No. CE170100004. K. M. is supported by King's College London through a Postgraduate International Scholarship. N. C. acknowledges support from National Science Foundation Grant No. PHY-1806990. M. S. is supported in part by the Science and Technology Facility Council (STFC), United Kingdom, under Research Grant No. ST/P000258/1. This paper has been given LIGO DCC number P2000258. Numerous software packages were used in this paper. These include MATPLOTLIB [42], NumPy [43], SciPy [44], BILBY [40], CPNest [39], ChainConsumer [45], and SEABORN [46].

APPENDIX: SIMULATED MAGNETIC NOISE PROPERTIES

We use low-noise magnetometers on site at the Advanced LIGO and Advanced Virgo detectors and correlate them to deduce what γ_{ij}^{M}, defined in Eq. (13), looks like. A discussion of the magnetometers and their locations is given in Ref. [20]. We use the real part of complex coherence (RPCC), defined as

$$\gamma_{ij}^{M}(f;t) = \mathrm{Re}\left[\frac{\tilde{m}_i^*(f;t)\tilde{m}_j(f;t)}{\sqrt{\tilde{m}_i^*(f;t)\tilde{m}_i(f;t)}\sqrt{\tilde{m}_j^*(f;t)\tilde{m}_j(f;t)}}\right], \tag{A1}$$

where $\tilde{m}_i(f;t)$ is the Fourier transform of the data from magnetometer i starting at time t evaluated at frequency f. We calculate the numerator and denominator of $\gamma_{ij}^{M}(f;t)$ separately over 4 s segments and average them separately over 1800 s of data to create an estimate of $\gamma_{ij}^{M}(f;t)$ for that 1800 s chunk of data. We do this for each 1800 s chunk of data available from July 9, 2019 00:00 UTC–September 7, 2019 00:00 UTC. We then take a histogram at each frequency over all of the 1800 s measurements. A heat map of this histogram is shown in Fig. 9 for each possible detector pair. For the simulations discussed in Sec. V, we use the median over the time chunks at each frequency, indicated by the white line in each panel in Fig. 9. This is indicated by the white line in Fig. 9.

The RPCC is not an exact measurement of $\gamma_{ij}^{\mathrm{M}}(f)$. It approximates this value only insofar as the "signal," $M(f)$, dominates the noise in the individual magnetometers. However, in the absence of a reliable analytic calculation (which is available in the GW case, for example), it is a good heuristic for capturing the sign and general shape of $\gamma_{ij}^{\mathrm{M}}(f)$.

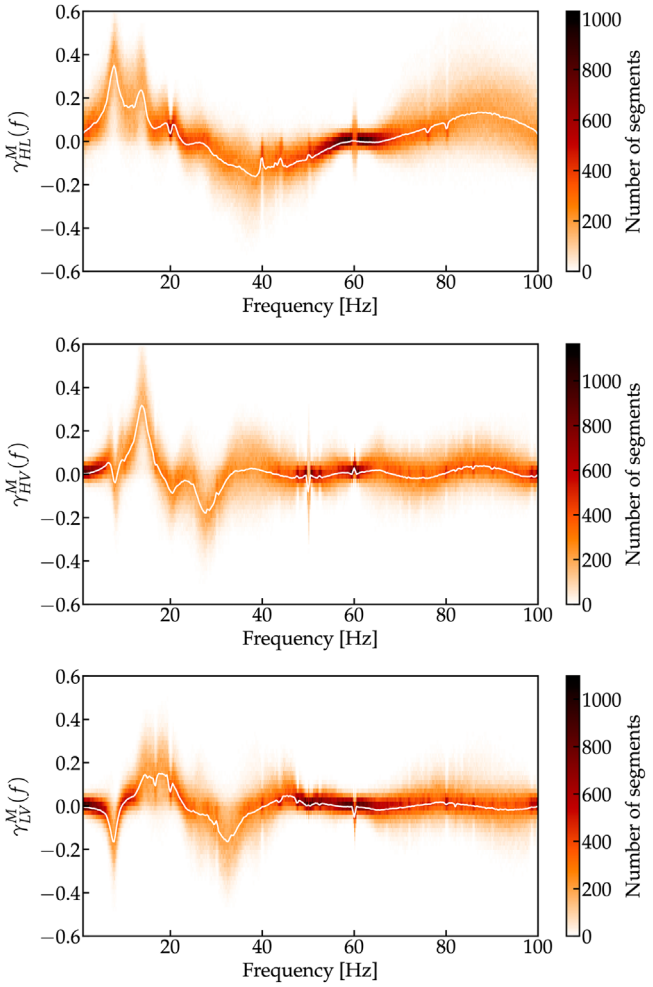

FIG. 9. Color indicates histogram of RPCC of Hanford-Livingston for each 1800 s chunk of data available for 60 days. The median value of all RPCC measurements taken at each frequency is shown in white.

[1] J. Aasi *et al.* (LIGO Scientific Collaboration), Advanced LIGO, Classical Quantum Gravity **32**, 074001 (2015), arXiv:1411.4547.

[2] F. Acernese *et al.* (VIRGO Collaboration), Advanced Virgo: A second-generation interferometric gravitational wave detector, Classical Quantum Gravity **32**, 024001 (2015).

[3] B. P. Abbott *et al.* (LIGO Scientific and Virgo Collaborations), GWTC-1: A Gravitational-Wave Transient Catalog of Compact Binary Mergers Observed by LIGO and Virgo during the First and Second Observing Runs, Phys. Rev. X **9**, 031040 (2019).

[4] See https://gracedb.ligo.org/superevents/public/O3/.

[5] B. P. Abbott *et al.* (LIGO Scientific and Virgo Collaborations), GW190425: Observation of a compact binary coalescence with total mass ~3.4 $M_{\odot}$, Astrophys. J. Lett. **892**, L3 (2020).

[6] R. Abbott *et al.*, GW190814: Gravitational waves from the coalescence of a 23 solar mass black hole with a 2.6 solar mass compact object, Astrophys. J. **896**, L44 (2020).

[7] B. P. Abbott *et al.* (LIGO Scientific and Virgo Collaborations), GW170817: Implications for the Stochastic Gravitational-Wave Background from Compact Binary Coalescences, Phys. Rev. Lett. **120**, 091101 (2018).

[8] N. Christensen, Stochastic gravitational wave backgrounds, Rep. Prog. Phys. **82**, 016903 (2019).

[9] B. P. Abbott *et al.* (LIGO Scientific and Virgo Collaborations), GW170814: A Three-Detector Observation of Gravitational Waves from a Binary Black Hole Coalescence, Phys. Rev. Lett. **119**, 141101 (2017).

[10] T. Callister, A. S. Biscoveanu, N. Christensen, M. Isi, A. Matas, O. Minazzoli, T. Regimbau, M. Sakellariadou, J. Tasson, and E. Thrane, Polarization-Based Tests of Gravity with the Stochastic Gravitational-Wave Background, Phys. Rev. X **7**, 041058 (2017).

[11] B. P. Abbott *et al.* (LIGO Scientific and Virgo Collaborations), Search for Tensor, Vector, and Scalar Polarizations in the Stochastic Gravitational-Wave Background, Phys. Rev. Lett. **120**, 201102 (2018).

[12] T. Callister, M. Fishbach, D. E. Holz, and W. M. Farr, Shouts and murmurs: Combining individual gravitational-wave sources with the stochastic background to measure the history of binary black hole mergers, Astrophys. J. **896**, L32 (2020).

[13] N. Christensen, Measuring the stochastic gravitational-radiation background with laser-interferometric antennas, Phys. Rev. D **46**, 5250 (1992).

[14] J. D. Romano and N. J. Cornish, Detection methods for stochastic gravitational-wave backgrounds: A unified treatment, Living Rev. Relativity **20**, 2 (2017).

[15] E. Thrane, N. Christensen, and R. M. S. Schofield, Correlated magnetic noise in global networks of gravitational-wave detectors: Observations and implications, Phys. Rev. D **87**, 123009 (2013).

[16] E. Thrane, N. Christensen, R. M. S. Schofield, and A. Effler, Correlated noise in networks of gravitational-wave detectors: Subtraction and mitigation, Phys. Rev. D **90**, 023013 (2014).

[17] Y. Himemoto and A. Taruya, Impact of correlated magnetic noise on the detection of stochastic gravitational waves: Estimation based on a simple analytical model, Phys. Rev. D **96**, 022004 (2017).

[18] Y. Himemoto and A. Taruya, Correlated magnetic noise from anisotropic lightning sources and the detection of stochastic gravitational waves, Phys. Rev. D **100**, 082001 (2019).

[19] M. W. Coughlin *et al.*, Subtraction of correlated noise in global networks of gravitational-wave interferometers, Classical Quantum Gravity **33**, 224003 (2016).

[20] M. W. Coughlin, A. Cirone, P. Meyers, S. Atsuta, V. Boschi, A. Chincarini *et al.*, Measurement and subtraction of Schumann resonances at gravitational-wave interferometers, Phys. Rev. D **97**, 102007 (2018).

[21] T. Callister, M. W. Coughlin, and J. B. Kanner, Gravitational-wave geodesy: A new tool for validating detection of the stochastic gravitational-wave background, Astrophys. J. Lett. **869**, L28 (2018).

[22] B. Allen and J. D. Romano, Detecting a stochastic background of gravitational radiation: Signal processing strategies and sensitivities, Phys. Rev. D **59**, 102001 (1999).

[23] C. M. F. Mingarelli, S. R. Taylor, B. S. Sathyaprakash, and W. M. Farr, Understanding $\Omega_{\rm gw}(f)$ in gravitational wave experiments, arXiv:1911.09745.

[24] B. P. Abbott *et al.*, Search for the isotropic stochastic background using data from Advanced LIGO's second observing run, Phys. Rev. D **100**, 061101 (2019).

[25] W. O. Schumann, On the radiationless natural oscillations of a conductive sphere surrounded by a layer of air and an ionospheric shell, Z. Naturforsch. Teil A **7**, 149 (1952).

[26] W. O. Schumann and H. König, On the observation of 'atmospherics' at low frequencies, Naturwissenschaften **41**, 183 (1954).

[27] C. Price, ELF electromagnetic waves from lightning: The Schumann resonances, Atmosphere-Ocean **7**, 116 (2016).

[28] D. D. Sentman, in *Handbook of Atmospheric Electrodynamics*, Vol. 1, edited by H. Volland (CRC Press, Boca Raton, 1995), p. 267.

[29] C. Price and A. Melnikov, Diurnal, seasonal and inter-annual variations in the Schumann resonance parameters, J. Atmos. Sol. Terr. Phys. **66**, 1179 (2004).

[30] H. Zhou, H. Yu, B. Cao, and X. Qiao, Diurnal, seasonal variations in the Schumann resonance parameters observed at chinese observatories, J. Atmos. Sol. Terr. Phys. **98**, 86 (2013).

[31] See https://alog.ligo-wa.caltech.edu/aLOG/index.php?callRep=39199.

[32] See https://logbook.virgo-gw.eu/virgo/?r=40025.

[33] G. Cella, C. N. Colacino, E. Cuoco, A. Di Virgilio, T. Regimbau, E. L. Robinson, and J. T. Whelan, Prospects for stochastic background searches using Virgo and LSC interferometers, Classical Quantum Gravity **24**, S639 (2007).

[34] B. P. Abbott *et al.*, Prospects for observing and localizing gravitational-wave transients with Advanced LIGO, Advanced Virgo and KAGRA, Living Rev. Relativity **21**, 3 (2018).

[35] V. Mandic, E. Thrane, S. Giampanis, and T. Regimbau, Parameter Estimation in Searches for the Stochastic Gravitational-Wave Background, Phys. Rev. Lett. **109**, 171102 (2012).

[36] W. R. Gilks, S. Richardson, and D. J. Spiegelhalter, *Markov Chain Monte Carlo in Practice* (CRC Press, Boca Raton, 1996).

[37] N. Christensen and R. Meyer, Markov chain Monte Carlo methods for Bayesian gravitational radiation data analysis, Phys. Rev. D **58**, 082001 (1998).

[38] J. Skilling, Nested sampling for general Bayesian computation, Bayesian Anal. **1**, 833 (2006).

[39] John Veitch, Walter Del Pozzo, Cody, Matt Pitkin, and ed1d1a8d, johnveitch/cpnest: Minor optimisation (2017), https://doi.org/10.5281/zenodo.835874.

[40] G. Ashton *et al.*, BILBY: A user-friendly Bayesian inference library for gravitational-wave astronomy, Astrophys. J. Suppl. Ser. **241**, 27 (2019).

[41] S. R. Cook, A. Gelman, and D. B. Rubin, Validation of software for Bayesian models using posterior quantiles, J. Comput. Graph. Stat. **15**, 675 (2006).

[42] J. D. Hunter, MATPLOTLIB: A 2D graphics environment, Comput. Sci. Eng. **9**, 90 (2007).

[43] S. van der Walt, S. C. Colbert, and G. Varoquaux, The NumPy array: A structure for efficient numerical computation, Comput. Sci. Eng. **13**, 22 (2011).

[44] P. Virtanen, R. Gommers, T. E. Oliphant, M. Haberland, T. Reddy, D. Cournapeau *et al.*, SciPy 1.0: Fundamental algorithms for scientific computing in PYTHON, Nat. Methods **17**, 261 (2020).

[45] S. R. Hinton, ChainConsumer, J. Open Source Softw. **1**, 00045 (2016).

[46] M. Waskom, O. Botvinnik, P. Hobson, J. B. Cole, Y. Halchenko, S. Hoyer *et al.*, computer code SEABORN, version 0.5.0, 2014.